BNL-107970-2015-JA

Mark C. Weidman[†], Kevin G. Yager[‡], William A. Tisdale[*,†]

[†]Department of Chemical Engineering, Massachusetts Institute of Technology, Cambridge, Massachusetts 02139, United States

[‡]Center for Functional Nanomaterials, Brookhaven National Laboratory, Upton, New York 11973, United States

KEYWORDS nanocrystal, interparticle spacing, self-assembly, ligand exchange, quantum dot, GISAXS

ABSTRACT: Controlling the interparticle spacing in quantum dot (QD) thin films is the most readily accessible way to control transport rates between neighboring QDs and a critical component of device optimization. Here, we use X-ray scattering measurements to accurately measure the interparticle spacing in films of highly monodisperse lead sulfide (PbS) QDs that have undergone a variety of device-relevant ligand exchanges. We tabulate these values for use in simulations and data analysis. We find that monothiol and dithiol ligand species typically result in interparticle spacing values that are equal to the length of a single monothiol or dithiol ligand. Additionally, we find that spin-coating a thick film of QDs followed by a long-duration ligand exchange results in a more complete ligand exchange than spin-coating many thin layers with short-duration ligand exchanges in between. The former method also preserves a remarkable degree of the long-range ordering that was present in the film prior to ligand exchange. These results shed light on ways to produce highly-ordered QD solids with compact and functional ligands, which could lead to enhanced interdot coupling and transport phenomena.

1. INTRODUCTION

Colloidal semiconductor nanocrystals, or quantum dots (QDs), are a promising group of materials for many optoelectronic applications.[1–4] These applications range from photovoltaics[4–6] to light-emitting diodes[2,7] to wavelength conversion.[8] For efficient operation, these diverse applications often require very different rates of transport between neighboring QDs. In photovoltaics it is desirable to maximize charge carrier extraction and transport between neighboring QDs[9] whereas in light conversion applications the aim is to isolate QDs from one another, typically by embedding them in a matrix.[10] Light-emitting diodes fall somewhere in between, seeking to balance charge transfer with efficient radiative recombination.[11] A readily accessible way to control the rates of transport in QD devices is by changing their surface ligand species to regulate their physical distance and electronic coupling.[11–13]

Here, we experimentally measure the interparticle spacing which is achieved for a variety of device-relevant ligand species for thin films made with highly monodisperse lead sulfide (PbS) QDs. We used grazing-incidence small-angle X-ray scattering (GISAXS), grazing-transmission small-angle X-ray scattering (GTSAXS), and wide-angle X-ray scattering (WAXS) to characterize both the interparticle spacing and the degree of ordering present in the film. We compare the results for two different methods of producing these films – one in which a thick film was spin-coated and then submerged in a ligand solution for 24 hours and one in which a layer-by-layer spin-coating approach was used to build a thick film from many thin layers. The two methods produce significantly different values for the achievable interparticle spacing as well as the degree of order which is maintained after the solid-state ligand exchange. We find that the submerged, long-duration ligand exchange on a relatively thick QD film produces a significantly smaller interparticle spacing than the short-duration ligand exchange on a relatively thin QD film. These results compliment the recent study of Kirmani *et al.*,[14] which demonstrates better photovoltaic performance can be achieved using fewer, thicker QD spin-coating steps and longer duration ligand exchanges. We find that a remarkably high degree of film order can be maintained, even when the ligand exchange constitutes a large loss in the film's volume. Additionally, interparticle spacing can be effectively controlled using varying chain length dithiols or monothiols and that the separation achieved is generally equal to the length of a single ligand species. We find that many of the ligands which offer enhanced performance in QD photovoltaics do not necessarily lead to the shortest interparticle spacing, which highlights the importance of energy-level matching and surface passivation in QD devices.[5,15,16] The interparticle spacing values tabulated here will be useful for simulations of QD films and data analysis. The ability to make QD superlattices with many types of compact and functionalized ligands demonstrated here could lead to enhanced coupling and the propensity for novel phenomena in these types of assemblies.[9]

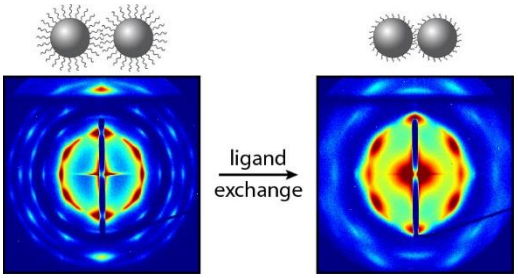

2. EXPERIMENTAL SECTION

Nanocrystal Synthesis. Monodisperse colloidal PbS QDs were synthesized according to the method detailed in our previous work.[17] We employed a large Pb:S precursor molar ratio (8:1 or greater) to achieve highly monodisperse QD ensembles. Lead (II) chloride (Alfa Aesar, 99.999%), sulfur (Sigma-Aldrich, ≥99.99%), oleylamine (Acros Organics, 80-90%), and oleic acid (Sigma-Aldrich, 90%) were used without further purification. Briefly, sulfur in oleylamine was heated to 120°C in an oil bath for 20 minutes with nitrogen bubbling through the solution.

The sulfur solution was then allowed to cool to room temperature, maintaining the nitrogen bubbling. The lead solution was prepared in a three neck flask by adding lead chloride to oleylamine. On a Schlenk line, the flask was degassed then heated under nitrogen to 120°C. At this point, the sulfur solution was swiftly injected into the lead solution, resulting in the formation of the PbS QDs. The reaction was held at 120°C for 1-30 minutes to access the different sizes of QDs studied here. To quench the reaction, the three neck cell was immersed in a water bath and cold hexanes were injected into the flask. The QD product was purified using alcohols and oleic acid followed by centrifugation to remove excess unreacted precursors and solvent. In all cases the oleylamine ligands on the QDs were exchanged for oleic acid ligands to improve colloidal stability.

Nanocrystal Characterization. Absorption spectra were measured using a Cary 5000 UV-Vis-NIR spectrophotometer. Photoluminescence emission spectra were collected using a BaySpec NIR spectrometer. The QDs were suspended at low concentrations in tetrachloroethylene for these measurements.

Scanning electron microscopy (SEM) was performed on a Zeiss Merlin operating at 20kV. Samples were the same as those used for X-ray scattering measurements (preparation detailed in the next section).

Transmission electron microscopy (TEM) was performed on a JEOL 2011 operating at 200 kV. Samples were prepared by drop casting QD suspensions in tetrachloroethylene onto TEM grids coated with an amorphous carbon support film.

X-ray diffraction (XRD) was performed on a Rigaku Smartlab with Cu Kα source operating at 45 kV and 200 mA.

Solution phase small-angle X-ray scattering (SAXS) was measured on a Rigaku Smartlab with Cu Kα source operating at 45 kV and 200 mA. Samples were prepared by filling glass capillaries with suspensions of QDs in toluene at concentrations of 50 mg/mL.

Sample Preparation. Thin films of QDs were deposited *via* spin-coating on 1x1 cm silicon wafers. All steps were performed in a nitrogen filled glovebox (less than 1 ppm oxygen and water). Prior to use, the silicon wafers were cleaned and treated overnight with a 0.02M (3-mercaptopropyl) trimethoxysilane solution in toluene to improve QD adhesion. QD films were deposited in one of two ways. In the first method, ~50 μL of a 50 mg/mL suspension of QDs in toluene was pipetted onto the silicon wafer. The wafer was then spun at 1,500 rpm for 30 seconds. This created a relatively thick QD film of ~15 nanocrystal layers. To exchange the ligands of this film, the silicon wafer was left for 24h in a 0.1M solution of the desired ligand in acetonitrile. Upon removal, the film was rinsed with pure acetonitrile to remove any excess ligand. In the second method, ~50 μL of a 10 mg/mL QD suspension in toluene was spin-coated onto a silicon wafer at 1,500 rpm for 30 seconds. This created a relatively thin film of ~3 nanocrystal layers. To exchange the ligands of this film, the surface of the film was flooded with a 0.1M solution of the desired ligand in acetonitrile. After 30 seconds of soaking, the ligand solution was spun off the sample at 1,500 rpm for 30 seconds. The surface of the film was then flooded with pure acetonitrile and spun at 1,500 rpm for 30 seconds. This process was repeated a total of 5 times in order to build a film of comparable thickness to the first method. For the hydrazine treatment, we use a 1M solution of hydrazine in methanol, as hydrazine in acetonitrile has been shown to remove only a small percentage of native oleate ligands in PbSe films.[18]

Ligand Species. 1-butanethiol (Sigma-Aldrich, 99%), 1-dodecanethiol (Sigma-Aldrich, ≥98%), 1-ethanethiol (Sigma-Aldrich, 97%), 1-hexanethiol (Sigma-Aldrich, 95%), 1-octanethiol (Sigma-Aldrich, ≥98.5%), 1-pentanethiol (Sigma-Aldrich, 98%), 1-propanethiol (Sigma-Aldrich, 99%), 1,2-ethanedithiol (Sigma-Aldrich, ≥98%), 1,3-benzenedithiol (Alfa Aesar, 97%), 1,4-butanedithiol (Sigma-Aldrich, 97%), 1,6-hexanedithiol (Sigma-Aldrich, 96%), 1,8-octanedithiol (Sigma-Aldrich, ≥97%), 1,10-decanedithiol (Alfa Aesar, 95%), 3-mercaptopropionic acid (Sigma-Aldrich, ≥99%), hydrazine (Sigma-Aldrich, 98%), and tetrabutylammonium iodide (Sigma-Aldrich, ≥99.0%) were used without further purification and immediately brought inside the glovebox upon arrival.

X-ray Scattering. Grazing-incidence small-angle X-ray scattering (GISAXS), grazing-transmission small-angle X-ray scattering (GTSAXS), and wide-angle X-ray scattering (WAXS) were performed at the undulator-based X9 beamline at the National Sychrotron Light Source at Brookhaven National Laboratory. For a thorough comparison of GISAXS and GTSAXS experimental techniques, please see Lu *et al.*[19] The X-ray energy was set to either 13.5 (0.9184 Å) or 14.1 keV (0.8793 Å), and the beam size was focused to 50 μm tall by 100 μm wide at the sample position using a KB mirror system.

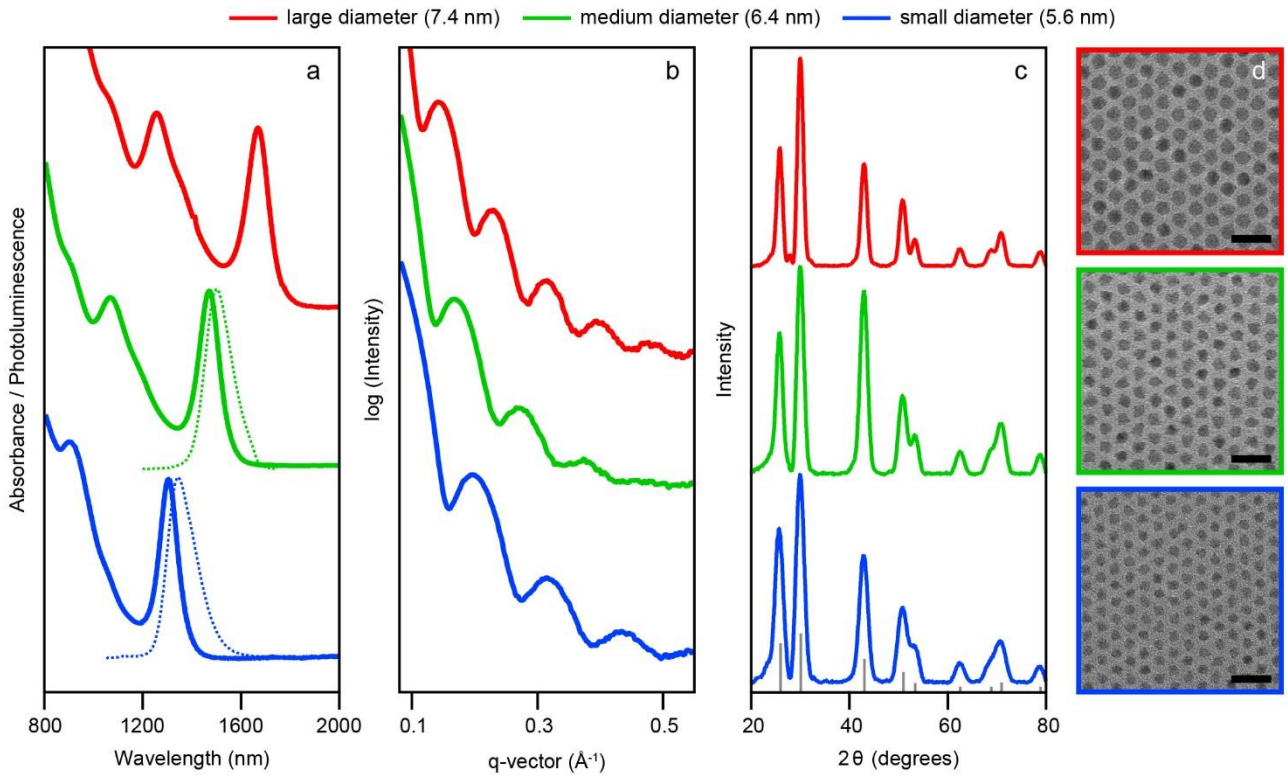

Figure 1. Characterization of the three sizes of PbS QDs used in this study. Data from the "large" diameter batch are shown in red, "medium" in green, and "small" in blue. All measurements have been normalized and offset for clarity. (a) Absorption (solid lines) and photoluminescence (dashed lines) spectra. (b) solution phase SAXS measurements. (c) XRD with reference PbS pattern (ICDD PDF number 00-005-0592) shown in gray. (d) TEM micrographs, scale bars are 20 nm.

The incident angle of the X-ray beam was varied from 0.08° to 0.30° for GISAXS and was set to 1.50° for GTSAXS. Due to the grazing-incidence, beam projection along the beam direction was ~1 cm in GISAXS measurements. For the GTSAXS measurements, the sample was positioned such that the center of the film was located in the beam-path. 2D scattering data were collected on CCD detectors that were calibrated using a silver behenate standard. Scattering patterns were indexed using in-house software. For quantifying interparticle spacing, the patterns were integrated azimuthally around the main beam. The scattering vector (q) is then converted to real-space (d) and a correction factor is applied based on whether the scattering peak comes from the (110) plane in BCC or (111) in FCC. For GISAXS measurements, we integrate the scattering intensity which occurs below the horizon of the substrate as it is less susceptible to the refraction and reflection effects that occur above the substrate horizon.[19] The reported interparticle spacing numbers are an average of the GISAXS data collected at 0.25° and 0.30° and the GTSAXS at 1.50°, when available, which generally show excellent agreement.

3. RESULTS AND DISCUSSION

To accurately measure interparticle spacing in QD thin films, we have synthesized three batches of monodisperse (size standard deviation < 3.5% of the mean diameter) PbS QDs using a previously reported method.[17] The three batches have core diameters of 5.6, 6.4, and 7.4 nm, which correspond to peak absorption values of 1305, 1470, and 1670 nm, respectively. Accordingly, they will be referred to as the nominally "small", "medium", and "large" diameter batches. We present the compiled properties of these QDs in Figure 1, with data being offset for clarity in panels a-c. Across the different measurements we have plotted the large diameter in red, the medium in green, and the small in blue. In Figure 1a we present the absorption spectra of the three sizes as well as the photolumniscence spectra from the small and medium diameter sizes. In Figure 1b we show the solution phase SAXS for the QDs dispersed in toluene. The well-defined absorption / photoluminescence spectra and the many oscillations in the solution phase SAXS verify the high monodispersity of the three ensembles. In Figure 1c we present the XRD patterns from the three batches as well as the reference peak locations for bulk PbS (gray). In Figure 1d we present TEM micrographs of the three sizes, highlighting that their core sizes differ by ~1 nm increments.

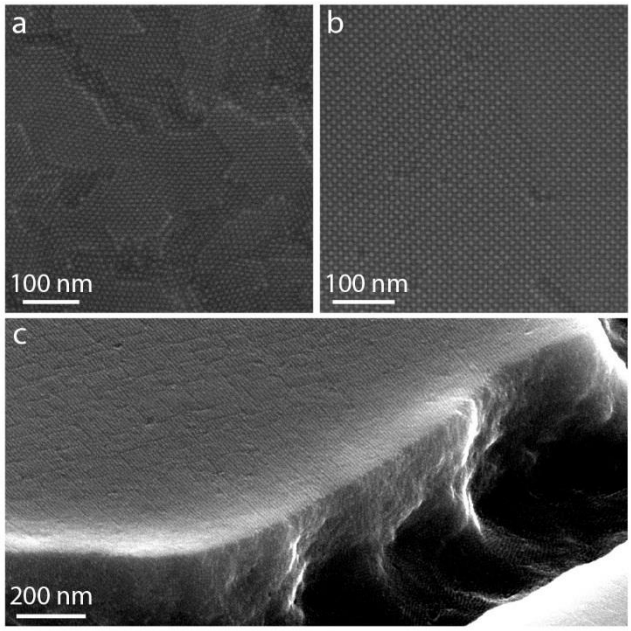

Figure 2. SEM micrographs of spin-coated QD films made from the large diameter QDs. (a) top-view of an exposed BCC (110) plane, (b) top-view of an exposed BCC (100) plane, and (c) horizon-view of a QD superlattice with exposed edge.

When spin-coated into thin film with their native oleic acid ligands, the QDs used in this study self-assemble into highly well-ordered superlattices. In Figure 2, we show SEM micrographs of these superlattices and their various orientations. In Figure 2a, the SEM image shows the (110) plane of a body-centered cubic (BCC) superlattice made using the large diameter QDs. The micrograph in Figure 2b is again a BCC superlattice made of large diameter QDs, but in this case with the (100) plane exposed. In Figure 2c, we present a horizon-view of the BCC superlattice, where it is possible to see the edge of the superlattice and the long-range nature of the self-assembly. We note that the images in Figure 2a and b also resemble the (111) and (100) planes in a face-centered cubic (FCC) superlattice. To distinguish between BCC and FCC superlattices, we use the X-ray scattering patterns from the same film, as described in the following section.

In Figure 3a, c, e we present the GTSAXS patterns from films made using these three QD sizes with their native oleic acid ligands. Unlike GISAXS, GTSAXS is less susceptible to experimental artifacts and distortion, so the full scattering pattern is visible and highly symmetric. Due to their monodispersity, the spin-coated films self-assemble into well-ordered superlattice structures. The peaks in the GTSAXS patterns have been indexed to identify the superlattice structure. The large diameter QDs (panel a) and small diameter QDs (panel e) index to a BCC superlattice with (110) planes parallel to the substrate. The medium diameter QDs (panel c) index to a FCC superlattice with (111) planes parallel to the substrate. It is unclear whether the driving force for self-assembly into BCC or FCC configurations is the result of slight differences in post-synthesis purification or due to the different relative facet areas present among the three core sizes.

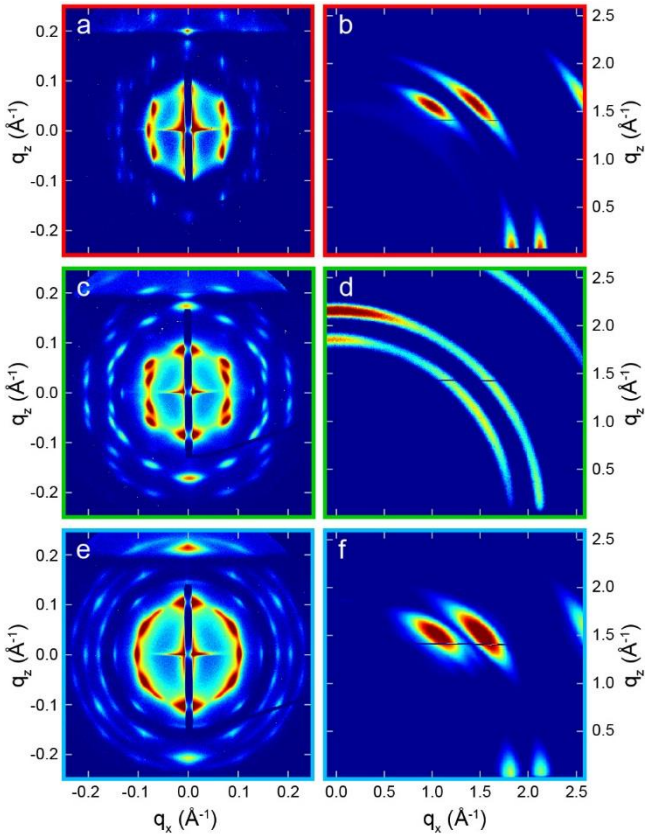

Figure 3. (a), (c), (e) GTSAXS patterns from spin-coated films of the three nanocrystal sizes: large diameter (red borders), medium diameter (green borders), and small diameter (blue borders). Corresponding SEM images of films made with the QD sizes are presented in (b), (d), and (f).

We note that similar behavior has been observed for PbS QDs by Choi *et al.*,[20] in which case air-exposure caused the transition from FCC to BCC packing. However, in our case, all QDs were exposed to air after synthesis, yet we observe FCC packing for the medium diameter QDs. We show the corresponding WAXS scattering patterns of these films in panels b, d, and f. The scattering in these images represent scattering from the (111), (200), and (220) PbS atomic planes, in going from low q-values to high q-values. The WAXS patterns in panels b and f show that the nanocrystals facets are coherently aligned within the BCC superlattice, while the more isotropic pattern in panel d indicates that the nanocrystals facets are not strongly aligned in the FCC packing. These observations are in agreement with Choi *et al.*, in which BCC superlattices result in oriented nanocrystals while FCC superlattices do not. The peaks in panel f are broader compared to those in panel b due to the smaller diameter of the nanocrystals being measured in panel f as compared to those used for panel b.

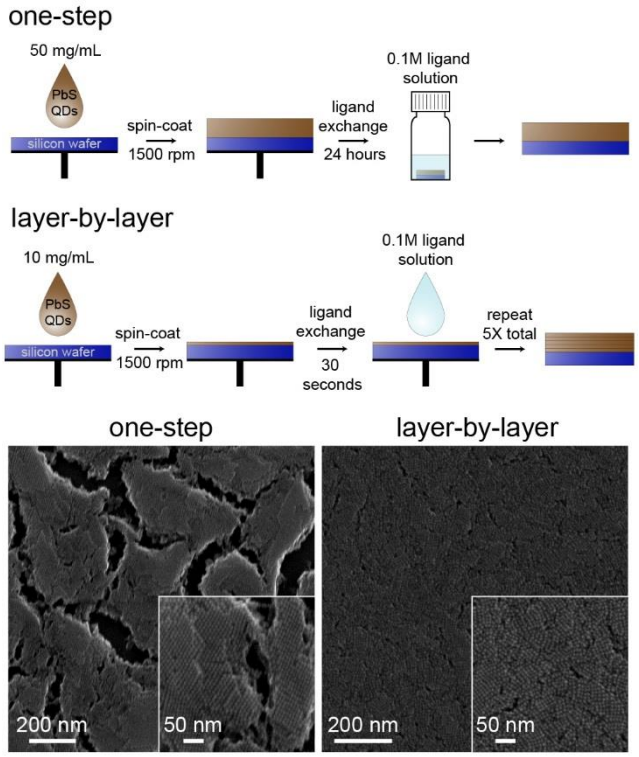

Figure 4. Diagram of the two film deposition methods studied here. The one-step method is characterized by a thick film and 24 hour ligand exchange while the layer-by-layer constitutes many thin layers with 30 second ligand exchanges in between. The SEM images show that while the layer-by-layer method creates a more homogenous film, the one-step method better preserves nanocrystal ordering.

The GTSAXS scattering patterns in Figure 3 and SEM images in Figure 2 show that spin-coating a film of QDs with native oleic acid ligands results in a highly-ordered superlattice with interparticle spacing of ~2.4 nm. We have chosen to study the effects of solid-state ligand exchange on the interparticle spacing and morphology of films such as these. To do so, we employed two different methods for making QD films, as detailed in Figure 4. In the first method, referred to as the "one-step" deposition, QDs are spin-coated onto a silicon wafer at a concentration of 50 mg/mL. This creates a relatively thick layer of QDs that is then left in a 0.1M solution of the desired ligand in acetonitrile for 24 hours. In the second method, referred to as the "layer-by-layer" deposition, QDs are spin-coated onto a silicon wafer at a concentration of 10 mg/mL. This creates a relatively thin film of QDs. The surface of the film is then flooded with a 0.1M solution of the desired ligand in acetonitrile and left to exchange for 30 seconds. This procedure is repeated a total of five times to build up a thick film. The layer-by-layer method is commonly used in literature for device fabrication.

In Figure 4 we also present SEM from 3-mercaptopropionic acid treated films made with the large diameter QDs. For the one-step deposition, we observed significant cracking in the film due to the loss of volume associated with the ligand exchange. However, the higher magnification inset shows that, despite the large loss in ligand volume, the ordering which was initially present in the spin-coated film (prior to ligand exchange) is well maintained even after the ligand exchange. In the layer-by-layer method, the overall film is more homogeneous, as repeated cycles serve to fill-in crack from the previous ligand exchange, but the SEM shows that only small domains (~10 nanocrystals) remain well-ordered when using this method.

In Figure 5, we highlight the major effects of core diameter and deposition method on the GISAXS patterns. To illustrate these trends, we use the scattering patterns from films with their native oleic acid ligands as well as films which have been treated with 1,8-octanedithiol, 1,4-butanedithiol, and 1,3-benzenedithiol using the two deposition methods. Starting with the scattering from the large diameter QD films, we see that nearly all the scattering peaks are maintained for the one-step method despite the 1 nm or greater shrinkage in the interparticle spacing. For the layer-by-layer method, scattering from the BCC (110) planes is observable, but the majority of higher ordering scattering is not present. This indicates that short-range ordering is occurring, but not on the extensive scale like that exhibited by oleic acid films or one-step deposition films. We see that this trend occurs for films made using the medium diameter and small diameter QDs as well. Therefore, we find that QD self-assembly is best maintained by spin-coating a thick film and doing a solid-state ligand exchange. In the layer-by-layer method, we hypothesize that short-range ordering is maintained within each spun layer, but that additional layers added on top of existing layers cannot form a cohesive superlattice. Furthermore, we find that the one-step method generally results in a shorter interparticle spacing, indicating a more effective ligand exchange has occurred. This result shows that the short exchange time in the layer-by-layer method (30 seconds), commonly used in device work, does not result in a complete ligand exchange. The one-step method produces a more complete exchange as a result of the longer duration and/or because submerging the film in the ligand solution is more affective at intercalating within the QD superlattice.

Focusing on the one-step deposition results for the different QD core size in Figure 5, we find that the large diameter QDs show the least change in going from their oleic acid scattering patterns to their ligand exchanged scattering patterns. A ligand exchange on a film made with the large diameter QDs constitutes a smaller change in the overall film volume than in a film made with the small diameter QDs. As expected, the film ordering is then least disrupted when the cores are large, with the medium size cores preserving order slightly better than the small size cores. Nevertheless, we still find that the one-step method produces films with many higher order reflections for both the small and medium diameter QDs.

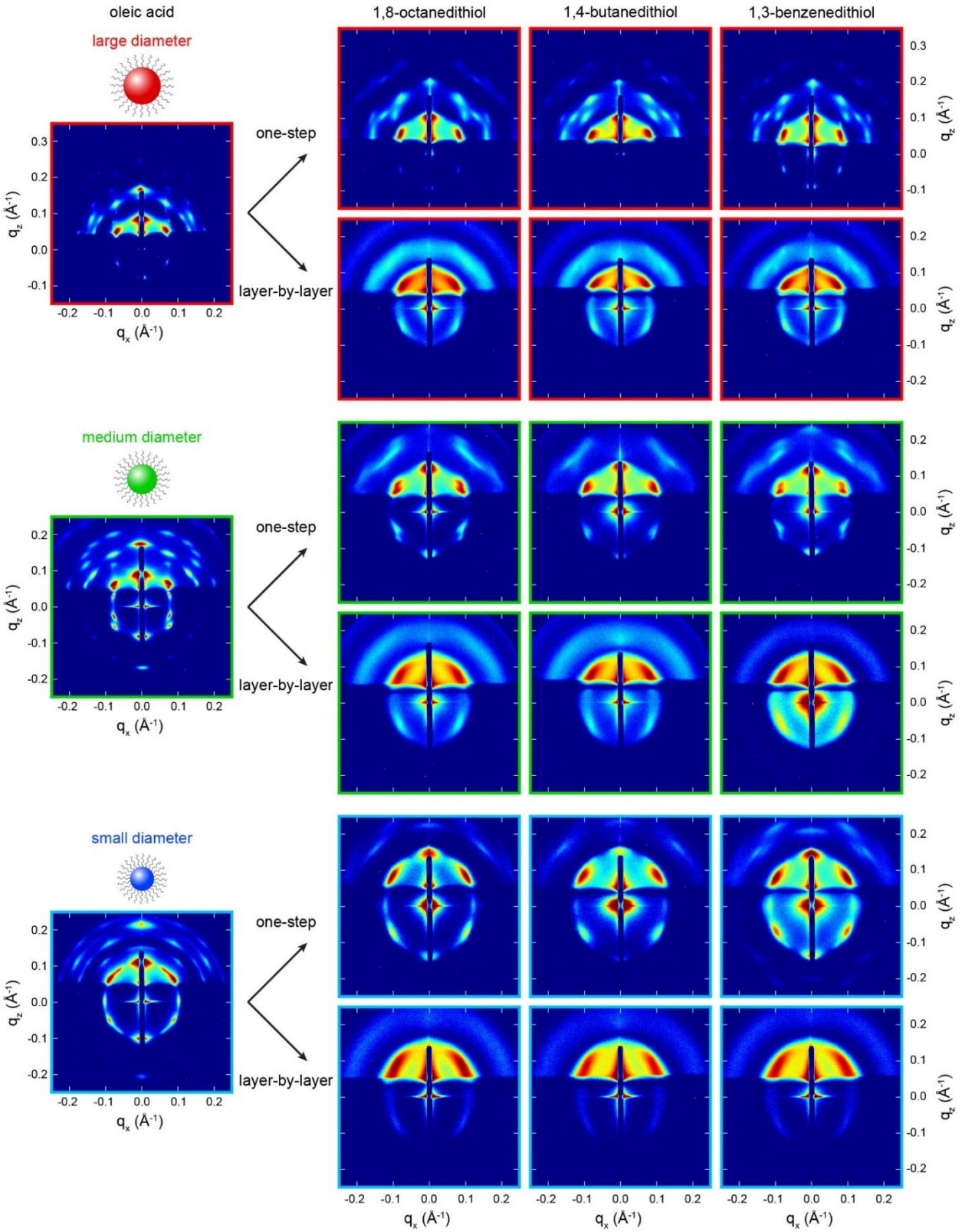

Figure 5. GISAXS patterns at an incident angle of 0.3° for all three sizes of QDs studied and made using the one-step method and the layer-by-layer method. From left to right the columns have ligands of oleic acid, 1,8-octanedithiol, 1,4-butanedithiol, and 1,3-benzenedithiol. Comparing between the different methods shows how ordering is better maintained using the one-step method while comparing between the different sizes of QDs shows that ordering is better maintained when the ligand volume constitutes a smaller fraction of the total volume.

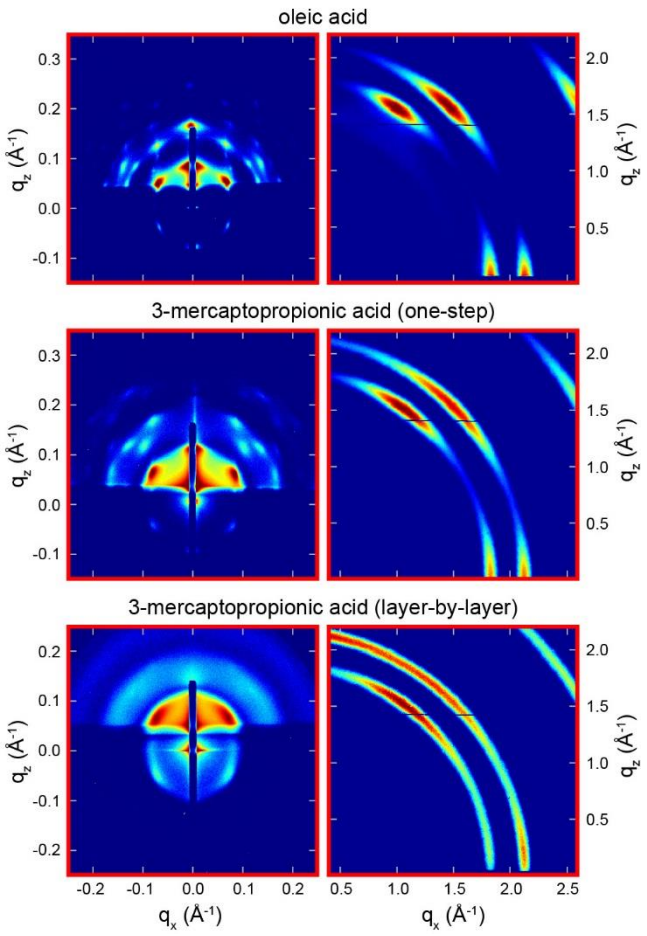

Figure 6. Comparison of the GISAXS patterns (left-hand column) and WAXS patterns (right-hand column) for films of large diameter QDs with oleic acid ligands and 3-mercaptopropionic acid ligands. The one-step method preserves the superlattice order and the cohesive nanocrystal facet arrangement better than the layer-by-layer method.

In Figure 6, we highlight some of the WAXS patterns with their corresponding GISAXS patterns, with all measurements having been taken with an incident beam angle of 0.30°. As shown in Figure 3, we find that the WAXS pattern is directional, which indicates that the individual nanocrystals are aligned with respect to one another. Using the 3-mercaptopropionic acid treatment as an example case, we see in Figure 6 that almost all of this nanocrystal alignment is maintained during the exchange from oleic acid to 3-mercaptopropionic acid when using the one-step deposition. For the large-diameter QDs shown in Figure 6, this constitutes an interparticle spacing change from 2.4 nm (with oleic acid) to 1.2 nm (with 3-mercaptopropionic acid). The loss in film volume is evidenced by the SEM image of this film, presented in Figure 4. Remarkably, we find that a device-relevant ligand species like 3-mercaptopropionic acid can replace the native ligands while still maintaining long range order and coherent nanocrystal alignment. For the layer-by-layer method, we observed some nanocrystal alignment in the WAXS patterns, but not to the same degree as when using the one-step method. We hypothesize that there is nanocrystal alignment during each spin-coat of natively capped QDs, but that there is no coherence between the five individual spin-coated layers of QDs. SEM images of this film are also shown in Figure 4.

In Table 1 we present the overall experimental interparticle spacing values measured for the ligand species studied and the two deposition methods studied. The presented values are the average interparticle spacing for the three different sizes of QD cores used. For a given sample, we have averaged the interparticle spacing measured at 0.25° and 0.30° (GISAXS) and at 1.50° (GTSAXS), when available. Additionally, we present one standard deviation, calculated from the interparticle spacing values of the three differently sized cores. We find that the standard deviation can represent a relatively large percentage of the average interparticle spacing value, particularly for the shorter ligands studied. The standard deviations reflect the variability in interparticle spacing among the three sizes of QDs studied. However, we do not observe any size-dependent trends in the interparticle spacing values and thus conclude that the variability may depend on other factors.

There are several interesting trends present in the data of Table 1. The first being that the one-step method consistently outperforms the layer-by-layer method in terms of the interparticle spacing reduction that is achievable. For easier comparison, we have included a difference column in which the one-step interparticle spacing value is subtracted from the layer-by-layer value. In all cases except for the longer thiols (1-dodecanemonothiol and 1,10-decanedithiol) and 1,3-benzenedithiol (only 0.1 nm difference between the two methods), the one-step method produces shorter interparticle spacing values. When the one-step method produces a shorter interparticle spacing, it is on average 0.4 nm less than the interparticle spacing of the layer-by-layer method. We therefore conclude that the one-step method, with its 24 hour, substrate-submerged ligand exchange, results in a more complete ligand exchange than the layer-by-layer method. Moving forward, we will focus on the one-step deposition interparticle spacing values, as they likely represent the interparticle spacing achieved with a complete ligand exchange.

Table 1. Interparticle spacing for the two deposition methods and ligand species studied.

	ligand	interparticle spacing (nm) one-step	layer-by-layer	difference (nm)
native	oleic acid	2.5 ± 0.5	2.3 ± 0.4	
	oleic acid (drop-cast)	2.4 ± 0.6	-	
monothiols	1-ethanemonothiol	0.4 ± 0.2	1.0 ± 0.2	0.6
	1-propanemonothiol	0.3 ± 0.2	0.8 ± 0.2	0.5
	1-butanemonothiol	0.5 ± 0.2	1.0 ± 0.2	0.5
	1-pentanemonothiol	0.4 ± 0.2	1.0 ± 0.3	0.6
	1-hexanemonothiol	0.8 ± 0.1	1.1 ± 0.3	0.3
	1-octanemonothiol	0.9 ± 0.3	1.2 ± 0.3	0.3
	1-dodecanemonothiol	1.9 ± 0.2	1.6 ± 0.2	-0.3
dithiols	1,2-ethanedithiol	1.0 ± 0.1	1.4 ± 0.1	0.4
	1,4-butanedithiol	0.7 ± 0.3	1.1 ± 0.3	0.4
	1,6-hexanedithiol	1.0 ± 0.2	1.2 ± 0.3	0.2
	1,8-octanedithiol	0.9 ± 0.3	1.1 ± 0.2	0.3
	1,10-decanedithiol	1.4 ± 0.5	1.2 ± 0.2	-0.1
miscellaneous	hydrazine (in methanol)	0.5 ± 0.4	1.1 ± 0.1	0.6
	tetrabutylammonium iodide	0.6 ± 0.1	1.3 ± 0.4	0.7
	3-mercaptopropionic acid	1.0 ± 0.3	1.3 ± 0.3	0.3
	1,3-benzenedithiol	1.2 ± 0.3	1.1 ± 0.3	-0.1

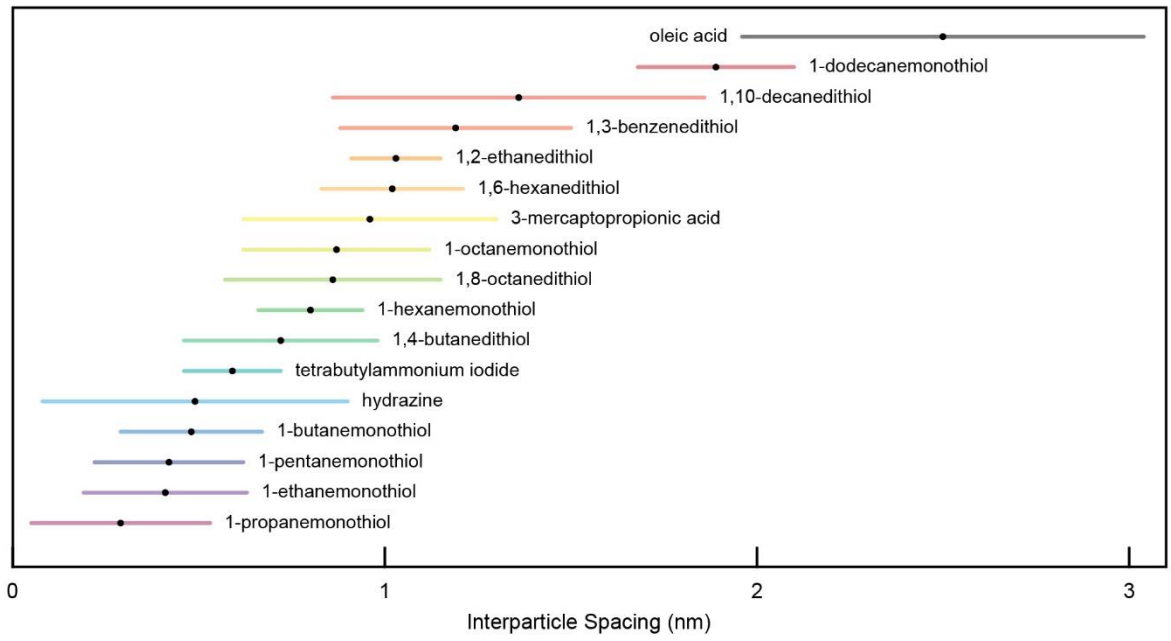

Figure 7. Interparticle spacing values for the ligand species studied, plotted from shortest to longest. The colored bars indicate the standard deviation among the three different core sizes used.

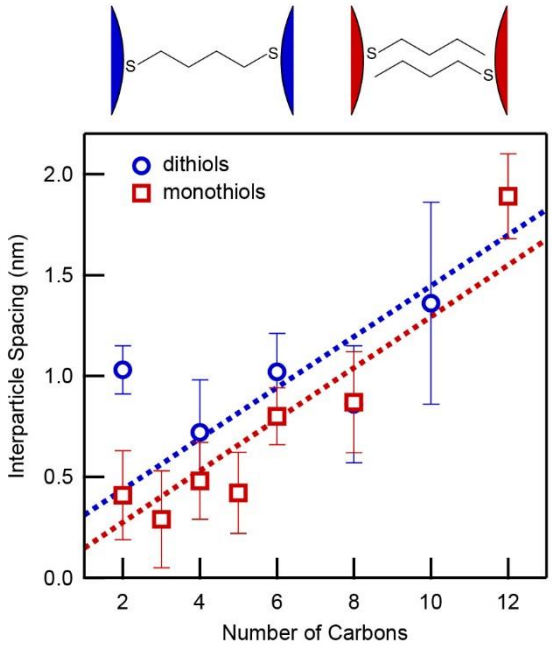

Figure 8. Experimental interparticle spacing as a function of number of carbons in the ligand for the dithiol and monothiol ligand species studied. The dashed lines are the simulated distances for these ligand species, as measured from sulfur to sulfur in the case of dithiols or sulfur to carbon in the case of monothiols (*i.e.* excluding hydrogen atoms).

The one-step deposition interparticle spacing values are shown in Figure 7, with the standard deviation represented by the colored bars. We see that the diverse lengths and species of ligands studied here offer a range of interparticle spacing tunability, from around 0.3 nm to 2.5 nm. Furthermore, we observe that many ligand types can offer a similar interparticle spacing. We find that the ligands which typically lead to high device performance in PbS photovoltaics (1,3-benzenedithiol[21], 3-mercaptopropionic acid[22], and tetrabutylammonium iodide[5]) are not the ligand species which provide the shortest interparticle spacing. This supports the notion that, in addition to interparticle spacing, it is also critical to consider surface passivation[22] and energetic alignment[15,16] when choosing a ligand for optimal device performance. It is also important to note that both 1,3-benzenedithiol and 3-mercaptopropionic acid produced some of the most well-ordered films studied (see Figures 5 and 6, respectively).

In Figure 8, we graphically represent the ligand spacing values of the monothiol series and dithiol series as a function of the number of carbon atoms in their chains. Additionally, the dashed lines represent the simulated ligand distance (ignoring the end hydrogen atoms) as determined using Chem3D Pro. The simulated dithiol length is systematically longer than the monothiol length due to the additional sulfur atom present. We see that both the dithiol and monothiols generally follow the trend that interparticle spacing increases as the ligand length increases, making both of these excellent candidates for tuning interparticle spacing. For the monothiols, we find that the experimental interparticle spacing values indicate that neighboring nanocrystals are separated by the length of a single monothiol ligand, as represented by the diagram at the top of Figure 7 (shown in red). In contrast, if neighboring nanocrystals were passivated by monothiols that did not interdigitate, we would expect the interparticle spacing values to be double the simulated ligand length. Our data supports the idea that the ligands of neighboring nanocrystals with monothiol ligand species do indeed interdigitate and thus result in an interparticle spacing value approximately equal to a single monothiol length.

The dithiol series in Figure 8 generally follows the simulated interparticle spacing for a single dithiol ligand between neighboring nanocrystals. This supports the notion that the dithiol species could be binding to the surface of two neighboring nanocrystals (as shown in blue in the diagram of Figure 8), however, we have not investigated further to prove this hypothesis. The dithiol interparticle spacing values are slightly larger than those for monothiol species with the same number of carbon atoms, which we attribute to the additional sulfur atom in the dithiol species. Despite this slightly larger interparticle spacing, we find that dithiols are excellent for maintaining film ordering and we highlight several of these in Figure 5. 1,2-ethanedithiol is a notable exception to the trends found in Figure 7. It is inconclusive whether this point is an outlier or whether it represents a case in which neighboring nanocrystals are separated by twice the ligand length of 1,2-ethanedithiol. We note as well that 1-ethanemonothiol produces an interparticle spacing value which is larger than that of 1-propanemonothiol. These findings suggest that, contrary to the diagrams in Figure 8, neighboring nanocrystals treated with 1,2-ethanedithiol and 1-ethanemonothiol may be separated by two ligand lengths. Interestingly, this observation could indicate a limit for how closely nanocrystals can be pulled together during a ligand exchange.

4. CONCLUSION

We have used three sizes of highly monodisperse PbS QDs to study the effects of solid-state ligand exchange on film morphology and interparticle spacing. Upon initial spin-coating with native oleic acid ligands, the QDs self-assemble into well-ordered BCC or FCC superlattices. Following conventional procedures for building thick films, we find that multiple spin-coating cycles with 30 second ligand exchanges in between layers does not preserve the long-range ordering of the film. Instead, by first spin-coating a single, thick layer of QDs and performing a substrate-submerged, 24 hour ligand exchange, we are able to maintain a remarkable degree of long-range ordering and to achieve a more complete ligand exchange, as evidenced by shorter interparticle spacing. By studying a size series of monothiol and dithiol ligand species, we conclude that the interparticle spacing achievable is generally equal to the length of a single dithiol or monothiol ligand.The interparticle spacing values tabulated here will be useful in simulations of QD solids as well as in the

analysis of data obtained from ligand-treated QD films. The one-step method sheds light on how it is possible to create well-ordered, nanocrystal-aligned QD solids with a variety of functional ligand species and tunable interparticle spacing.

AUTHOR INFORMATION

Corresponding Author

tisdale@mit.edu

Funding Sources

Any funds used to support the research of the manuscript should be placed here (per journal style).

Notes

The authors declare no competing financial interest.

ACKNOWLEDGMENT

The authors wish to thank N. Dahod and R. Hoffman for assistance with X-ray scattering measurements. We also thank M. Glassman and B. Olsen for helpful discussions. This work was primarily supported by the U.S. Department of Energy, Office of Basic Energy Sciences, under Award Number DE-SC0010538. M.C.W. was supported by a National Science Foundation Graduate Research Fellowship under Grant No. 1122374. GISAXS, GTSAXS, and WAXS measurements were performed at the Center for Functional Nanomaterials and the National Synchrotron Light Source, Brookhaven National Laboratory, which is supported by the U.S. Department of Energy, Office of Basic Energy Sciences, under Contract No. DE-AC02-98CH10886. TEM, XRD, SEM, and solution SAXS measurements were performed in the MRSEC Shared Experimental Facilities at MIT, supported by the National Science Foundation under award number DMR-08-19762.

REFERENCES

(1) Talapin, D. V; Lee, J.-S.; Kovalenko, M. V; Shevchenko, E. V. *Chem. Rev.* **2010**, *110*, 389–458.

(2) Supran, G. J.; Shirasaki, Y.; Song, K. W.; Caruge, J.-M.; Kazlas, P. T.; Coe-Sullivan, S.; Andrew, T. L.; Bawendi, M. G.; Bulović, V. *MRS Bull.* **2013**, *38*, 703–711.

(3) Shirasaki, Y.; Supran, G.; Bawendi, M.; Bulović, V. *Nat. Photonics* **2013**, *7*, 933–933.

(4) Lunt, R. R.; Osedach, T. P.; Brown, P. R.; Rowehl, J. A.; Bulović, V. *Adv. Mater.* **2011**, *23*, 5712–5727.

(5) Chuang, C. M.; Brown, P. R.; Bulović, V.; Bawendi, M. G. *Nat. Mater.* **2014**, 1–6.

(6) Ip, A. H.; Thon, S. M.; Hoogland, S.; Voznyy, O.; Zhitomirsky, D.; Debnath, R.; Levina, L.; Rollny, L. R.; Carey, G. H.; Fischer, A.; Kemp, K. W.; Kramer, I. J.; Ning, Z.; Labelle, A. J.; Chou, K. W.; Amassian, A.; Sargent, E. H. *Nat. Nanotechnol.* **2012**, *7*, 577–582.

(7) Cho, K.; Lee, E. K.; Joo, W.; Jang, E.; Kim, T.-H.; Lee, S. J.; Kwon, S.; Han, J. Y.; Kim, B.-K.; Choi, B. L.; Kim, J. M. *Nat. Photonics* **2009**, *3*, 341–345.

(8) Coe-Sullivan, S.; Liu, W.; Allen, P.; Steckel, J. S. *ECS J. Solid State Sci. Technol.* **2012**, *2*, R3026–R3030.

(9) Guyot-Sionnest, P. *J. Phys. Chem. Lett.* **2012**, *3*, 1169–1175.

(10) Lee, J.; Sundar, V. C.; Heine, J. R.; Bawendi, M. G.; Jensen, K. F. *Adv. Mater.* **2000**, *12*, 1102–1105.

(11) Sun, L.; Choi, J. J.; Stachnik, D.; Bartnik, A. C.; Hyun, B.-R.; Malliaras, G. G.; Hanrath, T.; Wise, F. W. *Nat. Nanotechnol.* **2012**, *7*, 369–373.

(12) Talapin, D. V.; Murray, C. B. *Science* **2005**, *310*, 86–89.

(13) Liu, Y.; Gibbs, M.; Puthussery, J.; Gaik, S.; Ihly, R.; Hillhouse, H. W.; Law, M. *Nano Lett.* **2010**, *10*, 1960–1969.

(14) Kirmani, A. R.; Carey, G. H.; Abdelsamie, M.; Yan, B.; Cha, D.; Rollny, L. R.; Cui, X.; Sargent, E. H.; Amassian, A. *Adv. Mater.* **2014**, 1–7.

(15) Brown, P. R.; Kim, D.; Lunt, R. R.; Zhao, N.; Bawendi, M. G.; Grossman, J. C.; Bulovic, V. *ACS Nano* **2014**.

(16) Scheele, M.; Hanifi, D.; Zherebetskyy, D.; Chourou, S. T.; Axnanda, S.; Rancatore, B. J.; Thorkelsson, K.; Xu, T.; Liu, Z.; Wang, L.-W.; Liu, Y.; Alivisatos, a P. *ACS Nano* **2014**, *8*, 2532–2540.

(17) Weidman, M. C.; Beck, M. E.; Hoffman, R. S.; Prins, F.; Tisdale, W. A. *ACS Nano* **2014**, 6363–6371.

(18) Law, M.; Luther, J. M.; Song, Q.; Hughes, B. K.; Perkins, C. L.; Nozik, A. J. *J. Am. Chem. Soc.* **2008**, *130*, 5974–5985.

(19) Lu, X.; Yager, K. G.; Johnston, D.; Black, C. T.; Ocko, B. M. *J. Appl. Crystallogr.* **2013**, *46*, 165–172.

(20) Choi, J. J.; Bealing, C. R.; Bian, K.; Hughes, K. J.; Zhang, W.; Smilgies, D.-M.; Hennig, R. G.; Engstrom, J. R.; Hanrath, T. *J. Am. Chem. Soc.* **2011**, *133*, 3131–3138.

(21) Brown, P. R.; Lunt, R. R.; Zhao, N.; Osedach, T. P.; Wanger, D. D.; Chang, L.-Y.; Bawendi, M. G.; Bulović, V. *Nano Lett.* **2011**, *11*, 2955–2961.

(22) Jeong, K. S.; Tang, J.; Liu, H.; Kim, J.; Schaefer, A. W.; Kemp, K.; Levina, L.; Wang, X.; Hoogland, S.; Debnath, R.; Brzozowski, L.; Sargent, E. H.; Asbury, J. B. *ACS Nano* **2012**, *6*, 89–99.